Journal Pre-proof

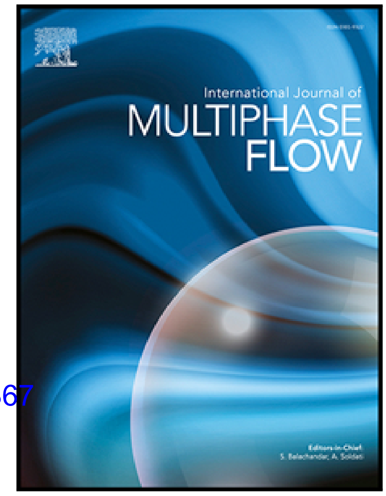

Whipping in gaseous flow focusing

S. Blanco-Trejo, M.A. Herrada, A.M. Gañán-Calvo, A. Rubio,
M.G. Cabezas, J.M. Montanero

PII: S0301-9322(20)30328-1
DOI: https://doi.org/10.1016/j.ijmultiphaseflow.2020.103367
Reference: IJMF 103367

To appear in: *International Journal of Multiphase Flow*

Received date: 13 April 2020
Revised date: 1 June 2020
Accepted date: 3 June 2020

Please cite this article as: S. Blanco-Trejo, M.A. Herrada, A.M. Gañán-Calvo, A. Rubio, M.G. Cabezas, J.M. Montanero, Whipping in gaseous flow focusing, *International Journal of Multiphase Flow* (2020), doi: https://doi.org/10.1016/j.ijmultiphaseflow.2020.103367

Highlights

- We describe the whipping instability in gaseous flow focusing.
- Whipping instability is explained in terms of the global stability analysis.
- We analyze the influence of the geometry on the whipping instability.

Whipping in gaseous flow focusing

S. Blanco-Trejo[a], M. A. Herrada[a], A. M. Gañán-Calvo[a], A. Rubio[b], M. G. Cabezas[b], J. M. Montanero[b,*]

[a]*Departamento de Ingeniería Aerospacial y Mecánica de Fluidos, Universidad de Sevilla, Camino de los Descubrimientos s/n 41092, Spain.*
[b]*Departamento de Ingeniería Mecánica, Energética y de los Materiales and Instituto de Computación Científica Avanzada (ICCAEx), Universidad de Extremadura, E-06006 Badajoz, Spain*

Abstract

We study both theoretically and experimentally the whipping instability in axisymmetric gaseous flow focusing realized in a converging-diverging nozzle. The lateral oscillation of both the tapering meniscus and emitted jet is explained in terms of the global linear instability of the lateral mode with the azimuthal number $m = 1$. A comparison with previous experiments shows good agreement. The distance between the feeding capillary and the nozzle neck hardly affects the $m = 1$ stability limit for the conditions considered in those experiments. We analyze the influence of the nozzle shape on the parameter conditions leading to whipping. As the nozzle convergence rate (the inverse of the length over which the diameter reduction takes place) increases, the flow becomes more stable under $m = 1$ perturbations. The above results are in marked contrast with those of the axisymmetric mode $m = 0$. For the axisymmetric mode, the minimum flow rate increases with the nozzle convergence rate, while the capillary-to-neck distance has considerable influence on the jetting-to-dripping transition. We also conduct experiments with different nozzles and capillary-to-neck distances to examine the effect of those factors on the stability of the jetting regime. The experiments allow us to distinguish between absolute whipping, in which both the tapering meniscus and the emitted jet oscillate, and convective whipping, in which the jet oscillates while the meniscus remains practically steady. Absolute whipping is observed for water and 1-cSt silicone oil focused with the nozzle with the smallest convergence rate and capillary-to-neck distance. The increase of the liquid viscosity stabilizes the liquid meniscus, producing the transition from absolute to convective whipping. In the high-viscosity case, the oscillation of the emitted jet far away from the discharge orifice is considerably affected by the shape of the nozzle in front of its neck. In fact, the increase of the convergence rate and capillary-to-neck distance eliminates the convective whipping as well. The reduction of surface tension enhances absolute whipping. We explain the appearance of the two types of whipping in terms of the flow pattern induced

*Corresponding author: J. M. Montanero (jmm@unex.es)

by the nozzle shape in front of the neck.

Keywords: gaseous flow focusing, whipping instability, global stability analysis, micronozzles

1. Introduction

The production of microjets has enormous applications in very diverse fields such as biotechnology, analytical chemistry, pharmacy and food industry, and industrial engineering. These capillary structures are the natural gate to produce drops, emulsions, and capsules on the micrometer scale, in a continuous way, and with a relatively large degree of monodispersity (Eggers and Villermaux, 2008). The so-called tip streaming phenomenon allows for the reduction of the capillary jet diameter down to the micrometer scale while keeping the size of the passages and orifices of the ejector on the scale of hundreds of microns (Montanero and Gañán-Calvo, 2020). Several tip streaming configurations can be used to produce very thin liquid jets (Taylor, 1964; Eggers, 1997; Cohen et al., 2001; Collins et al., 2008; Castro-Hernández et al., 2009; Anna and Mayer, 2006). In aerodynamic (gaseous) flow focusing (Gañán-Calvo, 1998), the liquid is supplied across a feeding capillary at a flow rate of the order of a few microliters per minute. The feeding capillary is placed in front of a discharge orifice whose diameter is commensurate with that of the capillary. A high-speed gaseous current coflows with the liquid across the discharge orifice. The combination of the pressure drop and viscous shear stress caused by the gaseous current drives the liquid flow, stretching the meniscus attached to the feeding capillary. A thin jet tapers from the meniscus tip and exits the ejector together with the outer gaseous stream. The original plate-orifice flow focusing configuration (Gañán-Calvo, 1998) was modified by DePonte et al. (2008) ten years later by replacing the plate with a borosilicate tube inside which the feeding capillary was introduced. The tube was ended by a fire-shaped nozzle to produce the same focusing effect as that of the plate orifice in the original configuration. DePonte et al. (2008) coined the expression “Gas Dynamic Virtual Nozzle” (GDVN) to refer to this ejector.

Gaseous flow focusing has found applications in very diverse fields. For instance, microparticles of complex structures have been produced by injecting coaxially two immiscible liquid streams (Gañán-Calvo et al., 2013). Viscoelastic threads (Ponce-Torres et al., 2016; Hofmann et al., 2018; Vasireddi et al., 2019) for smooth printing and bioplotting (Ponce-Torres et al., 2017) have been produced by applying essentially the flow focusing principle. Ponce-Torres et al. (2019) have recently extruded fibers with diameters ranging from a few microns down to hundreds of nanometers with the gaseous flow focusing spinning method. A gaseous co-flow focusing process has been used to produce stimuli-responsive microbubbles that comprise perfluorocarbon suspension of silver nanoparticles in a lipid (Si et al., 2016). In electro-flow focusing (Gañán-Calvo et al., 2006), a relatively small voltage is applied to the liquid to charge the droplets, which make them perfect candidates for surface sample desorption (Forbes and Sisco, 2014a,b).

Among the several gaseous flow focusing applications, the serial femtosecond crystallography (SFX) is probably the most important one. In fact, this technology has revolutionized the molecular determination of complex biochemical species by recording single flash diffraction patterns of many individual protein crystals (Chapman *et al.*, 2011). Most experiments in SFX have utilized a liquid microjet to place the sample into the beam focus. The jet must be perfectly steady to ensure a consistent interaction with the X-ray beam, which allows for efficient data collection. The protein crystals are damaged by the beam, and therefore the jet must be sufficiently fast to ensure that the exposed sample exits the interaction region before the next pulse strikes the jet Stan *et al.* (2016). In fact, a fresh sample must be placed into the beam focus at a rate that matches the arrival of X-ray pulses. This constitutes a severe condition for, e.g., the European XFEL, which produces pulses at frequencies of the order of 10^6 Hz (Wiedorn *et al.*, 2018). The X-ray pulse produces an explosion of the liquid in the interaction region, which must be located sufficiently far from the nozzle exit to avoid a rapid collection of sputtered material from the explosion. In addition, the jet must be as thin as possible to reduce the background diffraction signal. The simultaneous fulfillment of these two last conditions is a difficult task because surface tension shortens the jet as the diameter decreases. In SFX, the jet is usually generated by aerodynamically focusing (Gañán-Calvo, 1998; DePonte et al., 2008; Zahoor et al., 2018) a liquid stream with a GDVN-like ejector. The production of long and thin jets imposes severe constraints on the geometrical design of issuing nozzles (DePonte et al., 2008; Beyerlein et al., 2015; Piotter et al., 2018; Wiedorn *et al.*, 2018).

For a given geometrical configuration, the size of the focused jet can be reduced either by decreasing the liquid flow rate or by increasing the pressure drop applied to the gas stream. In the first case, one inevitably runs into an axisymmetric instability leading to the dripping regime (Si et al., 2009; Vega et al., 2010). In the latter case, the steady jetting mode becomes unstable due to the growth of whipping (bending) oscillations (Chigier and Reitz, 1996; Lasheras and Hopfinger, 2000) of the capillary system. In the whipping instability, surface tension has a stabilizing effect, and the destabilizing factor is purely aerodynamic: a perturbation at the jet free surface causes the gas stream to accelerate as it passes a crest, lowering the pressure at that point and encouraging the crest to increase in size (as in wind-generated ripples on a liquid free surface). The analysis of the whipping instability entails certain complexity even for a parallel liquid base flow. In fact, an accurate calculation of the perturbation growth rate requires the consideration of the gas viscosity even for small values of this parameter because the existence of an outer boundary layer significantly affects the instability (Gordillo and Pérez-Saborid, 2005). The problem for non-parallel liquid flows (as those produced by flow focusing) becomes much more complicated due to the cumbersome numerics. However, this analysis is highly relevant to optimize the production of both microdroplets and microfibers from jetting realizations.

In the classical plate-orifice configuration, the whipping instability is found in the jet beyond the discharge orifice, does not propagate upstream, and, therefore, the liquid meniscus remains perfectly steady (convective whipping). On the contrary, when the jet is focused by a nozzle (as happens in SFX) (DePonte et al., 2008), the liquid meniscus can also oscillate laterally (absolute whipping) (Acero et al., 2012). In some cases, those oscillations make the liquid touch the inner wall of the nozzle, which constitutes a serious obstacle in applications. Acero et al. (2012) speculated that the absence of absolute whipping in the plate-orifice configuration might be due to the radial character of the gaseous flow in front of the discharge orifice, which somehow stabilizes the meniscus under bending perturbations. Neither the origin of this phenomenon nor the way to eliminate it has been determined yet.

In the linear global stability analysis (Theofilis, 2011), we calculate the base flow characterizing the steady jetting mode of a certain capillary system. Then, we interrogate the base flow about its response to small-amplitude perturbations (Sauter and Buggisch, 2005; Tammisola et al., 2012; Gordillo et al., 2014; Dharmansh and Chokshi, 2016, 2017). The system evolves asymptotically (i.e., for sufficiently large times) dominated by the mode with the largest growth rate of the eigenfrequency spectrum. If this growth rate is positive, then natural perturbations lead to the base flow instability. Cruz-Mazo et al. (2017) have shown that this occurs to axisymmetric perturbations in gaseous flow focusing for sufficiently large applied pressure drops and flow rates below a minimum value. In this work, we apply the same methodology to explain the whipping instability arising for sufficiently large pressure drops. We hypothesize that the lateral oscillation of the liquid meniscus and/or emitted jet observed in experiments (Acero et al., 2012) corresponds to the growth of the dominant $m = 1$ linear mode. To the best of our knowledge, the non-axisymmetric ($m \neq 0$) global stability analysis has not as yet been applied to any capillary systems. In fact, previous studies of non-axisymmetric perturbations are restricted to local stability analyses, which assume that the base flow is quasi-uniform in the streamwise direction over a distance of the order of the wavelength of the dominant perturbation (Montanero and Gañán-Calvo, 2020). This approximation is not valid to examine the dynamical response of the flow focusing meniscus.

In this work, we will study the appearance of the whipping instability in gaseous flow focusing both theoretically and experimentally. In the numerical analysis, the steady base flow will be calculated by solving the non-linear, steady Navier-Stokes equations. Then, the linear eigenmodes will be obtained to examine the response of that flow to small-amplitude perturbations. The parameter conditions leading to whipping are assumed to be those for which the $m = 1$ dominant eigenmode grows on time. In the experimental study, we will determine the parameter conditions for which convective and absolute whipping come up. We will consider different nozzle shapes and capillary-to-neck distances both in the global stability analysis and in the experiments. We will focus on the nozzle convergence rate, defined as the inverse of the distance along which the diameter reduces to its minimum value. The results will show that whipping is suppressed as the convergence rate increases, which explains

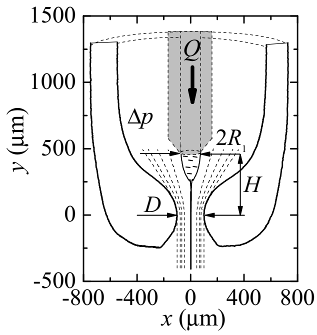

Figure 1: Axisymmetric gaseous flow focusing. The geometrical configuration corresponds to that used in the experiments by Acero et al. (2012). The values of the main parameters are $R_1 \simeq 75$ μm, $D \simeq 200$ μm, and $H \simeq 440$ μm.

why whipping is much less common in the classical plate-orifice configuration (Gañán-Calvo, 1998).

The paper is organized as follows. Section 2 presents the governing equations and briefly describes the numerical method. The experimental procedure is explained in Sec. 3. Section 4 shows both the theoretical and experimental results. The paper closes with some concluding remarks in Sec. 5.

2. Theoretical method

The gaseous flow focusing configuration considered in this paper is shown in Fig. 1. A liquid of density ρ_ℓ and viscosity μ_ℓ is injected through a feeding capillary of radius R_1 at a constant flow rate Q. The feeding capillary is located inside a converging-diverging nozzle at a distance H from the nozzle neck, whose diameter is D. A pressure drop Δp is applied to a gas stream of density ρ_g and viscosity μ_g. The gas stream stretches the liquid meniscus that hangs on the edge of the capillary end due to the action of the surface tension σ. In the steady jetting regime, the meniscus tip emits a liquid microjet, which crosses the nozzle coflowing with the outer gas stream.

In this section, all the variables are made dimensionless with the capillary radius R_1, the liquid density ρ_ℓ, and the surface tension σ, which yields the characteristic time, velocity and pressure scales $t_c = (\rho_\ell R_1^3/\sigma)^{1/2}$, $v_c = R_1/t_c$, and $p_c = \sigma/R_1$, respectively. The velocity $\mathbf{v}^{(j)}(r, z, \theta; t) = U^{(j)}(r, \theta, z; t)\ \mathbf{e_r} + V^{(j)}(r, \theta, z; t)\ \mathbf{e}_\theta + W^{(j)}(r, \theta, z; t)\ \mathbf{e_z}$ and pressure $p^{(j)}(r, \theta, z; t)$ fields verify the Navier-Stokes equations:

$$\frac{(rU^{(j)})_r}{r} + \frac{V_\theta^{(j)}}{r} + W_z^{(j)} = 0 \,, \tag{1}$$

$$\rho^{\delta_{jg}}\left(U_t^{(j)}+U^{(j)}U_r^{(j)}+V^{(j)}\frac{U_\theta^{(j)}}{r}+W^{(j)}U_z^{(j)}-\frac{V^{(j)2}}{r}\right)=$$
$$-p_r^{(j)}+\mu^{\delta_{jg}}\,Oh\left[\frac{(rU_r^{(j)})_r}{r}+\frac{U_{\theta\theta}^{(j)}}{r^2}+U_{zz}^{(j)}-\frac{U^{(j)}}{r^2}-\frac{2V_\theta^{(j)}}{r^2}\right]\ , \qquad (2)$$

$$\rho^{\delta_{jg}}\left(V_t^{(j)}+U^{(j)}V_r^{(j)}+\frac{U^{(j)}V^{(j)}}{r}+V^{(j)}\frac{V_\theta^{(j)}}{r}+W^{(j)}V_z^{(j)}\right)=$$
$$-p_\theta^{(j)}+\mu^{\delta_{jg}}\,Oh\left[\frac{(rV_r^{(j)})_r}{r}+\frac{V_{\theta\theta}^{(j)}}{r^2}+V_{zz}^{(j)}-\frac{V^{(j)}}{r^2}+\frac{2U_\theta^{(j)}}{r^2}\right]\ , \qquad (3)$$

$$\rho^{\delta_{jg}}\left(W_t^{(j)}+U^{(j)}W_r^{(j)}+V^{(j)}\frac{W_\theta^{(j)}}{r}+W^{(j)}W_z^{(j)}\right)=$$
$$-p_z^{(j)}+\mu^{\delta_{jg}}\,Oh\left[\frac{(rW_r^{(j)})_r}{r}+\frac{W_{\theta\theta}^{(j)}}{r^2}+W_{zz}^{(j)}\right]\ . \qquad (4)$$

In the above equations, $\rho=\rho_g/\rho_\ell$ and $\mu=\mu_g/\mu_\ell$ are the density and viscosity ratios, δ_{km} is the Kronecker delta, the superscripts $j=\ell$ and g refer to the liquid and gas phases, respectively, the subscripts t, r, and z denote the partial derivatives with respect to the corresponding variables, and $Oh=\mu_\ell(\rho_\ell\sigma R_1)^{-1/2}$ is the Ohnesorge number. It is worth noting that, although the density and viscosity ratios take very small values in gaseous flow focusing, they may significantly affect the lateral (whipping) instability of the steady jetting regime (Gordillo and Pérez-Saborid, 2005; Herrada et al., 2010).

The Navier-Stokes equations are integrated considering the kinematic compatibility condition at the free surface position $r=F(\theta,z;t)$:

$$F_t-U^{(j)}+\frac{F_\theta}{F}V^{(j)}+F_zW^{(j)}=0\ . \qquad (5)$$

The balance between the normal and tangential stresses on the two sides of the free surface reads

$$\tau_n^{(\ell)}=\tau_n^{(g)}\ ,\quad \tau_{t_1}^{(\ell)}=\tau_{t_1}^{(g)}\ ,\quad \tau_{t_2}^{(\ell)}=\tau_{t_2}^{(g)}, \qquad (6)$$

where $\tau_n^{(j)}$, $\tau_{t1}^{(j)}$ and $\tau_{t2}^{(j)}$ are the sum of capillary pressure, hydrostatic pressure and viscous stress on the two sides of the free surface, and the subindexes n, t_1 and t_2 denote the normal and two tangential directions, respectively. These stresses are given by the expressions

$$\tau_n^{(j)}=p^{(j)}-\nabla\cdot\mathbf{e_n}-\frac{2\mu^{\delta_{jg}}\,Oh}{C_n^2}\left\{U_r^{(j)}+F_z\left(F_zW_z^{(j)}-U_z^{(j)}-W_r^{(j)}\right)\right.$$
$$\left.-\frac{F_\theta}{F}\left[-\frac{F_\theta}{F^2}\left(U^{(j)}+V_\theta^{(j)}\right)+\frac{U_\theta^{(j)}}{F}+V_r^{(j)}-\frac{V^{(j)}}{F}-F_z\left(V_z^{(j)}+\frac{W_\theta^{(j)}}{F}\right)\right]\right\}, \qquad (7)$$

$$\tau_{t1}^{(j)} = \frac{\mu^{\delta_{jg}} Oh}{C_n C_t}\left\{2F_z\left(U_r^{(j)} - W_z^{(j)}\right) + \left(1-F_z^2\right)\left(W_r^{(j)} + U_z^{(j)}\right)\right.$$
$$\left. -\frac{F_\theta}{F}\left[V_z^{(j)} + \frac{W_\theta^{(j)}}{F} + F_z\left(\frac{U_\theta^{(j)}}{F} + V_r^{(j)} - \frac{V^{(j)}}{F}\right)\right]\right\}, \qquad (8)$$

$$\tau_{t2}^{(j)} = \frac{\mu^{\delta_{jg}} Oh}{C_n^2 C_t}\left\{\frac{2F_\theta}{F}\left[U_r^{(j)} - \left(1+F_z^2\right)\frac{U^{(j)} + V_\theta^{(j)}}{F} + F_z\left(F_z W_z^{(j)} - U_z^{(j)} - W_r^{(j)}\right)\right]\right.$$
$$\left. + \left(1+F_z^2 - \frac{F_\theta^2}{F^2}\right)\left[\frac{U_\theta^{(j)}}{F} + V_r^{(j)} - \frac{V^{(j)}}{F} - F_z\left(V_z^{(j)} + \frac{W_\theta^{(j)}}{F}\right)\right]\right\}, \qquad (9)$$

where C_n, C_t, C_θ are functions of the instantaneous free surface shape given by the equations

$$C_n = \left(1 + \frac{F_\theta^2}{F^2} + F_z^2\right)^{1/2}, \quad C_t = \left(1+F_z^2\right)^{1/2}, \quad C_\theta = \left(1 + \frac{F_\theta^2}{F^2}\right)^{1/2}. \qquad (10)$$

In addition, $\mathbf{e_n} = \frac{1}{FC_n}\left[(F_\theta \sin\theta + F\cos\theta)\,\mathbf{e_r} - (F_\theta\cos\theta + F\sin\theta)\,\mathbf{e}_\theta - FF_z\,\mathbf{e_z}\right]$ is the outward unit vector perpendicular to the free surface, and

$$\nabla\cdot\mathbf{e_n} = \frac{1}{FC_n} + \frac{1}{FC_n^3}\left[\frac{F_\theta}{F}\left(\frac{F_\theta}{F} + 2F_z F_{\theta z}\right) - C_t^2\frac{F_{\theta\theta}}{F} - C_\theta^2 F F_{zz}\right] \qquad (11)$$

is the local mean curvature. The anchorage condition $F = 1$ is imposed at the edge of the feeding capillary, while the no-slip boundary conditions $\mathbf{v} = \mathbf{0}$ is prescribed on all the solid surfaces. Periodic boundary conditions in the angular direction are imposed for all the variables.

We impose the Hagen-Poiseuille velocity distribution, $U^{(\ell)} = 0$ and $W^{(\ell)} = 2v_e(1-r^2)$ ($v_e = Q/(\pi R_1^2 v_c)$), and a uniform velocity profile at the inlet sections $z = 0$ of the liquid and gas domains, respectively. We set uniform pressures at the outlet sections of the gas and liquid domains. The liquid outlet pressure equals that of the gas plus the capillary pressure. The pressure drop Δp applied to the gas stream is calculated as the difference between the value averaged over the inlet section and that imposed at the outlet section.

The steady and axisymmetric base flow is characterized by the velocity and pressure fields, $\mathbf{v}_b(r,z) = U_b(r,z)\,\mathbf{e_r} + W_b(r,z)\,\mathbf{e_z}$ and $p_b(r,z)$, as well as by the distance $F_b(z)$ between a surface element and the z axis. To calculate the linear global modes, one assumes the spatio-temporal dependence

$$U(r,\theta,z;t) = U_b(r,z) + \epsilon\,\hat{U}(r,z)\,e^{-i\omega t + im\theta}, \qquad (12)$$

$$V(r,\theta,z;t) = \epsilon\,\hat{V}(r,z)\,e^{-i\omega t + im\theta}, \qquad (13)$$

$$W(r,\theta,z;t) = W_b(r,z) + \epsilon\,\hat{W}(r,z)\,e^{-i\omega t+im\theta}, \tag{14}$$

$$p(r,\theta,z;t) = p_b(r,z) + \epsilon\,\hat{p}(r,z)\,e^{-i\omega t+im\theta}, \tag{15}$$

$$F(\theta,z;t) = F_b(z) + \epsilon\,\hat{F}(z)\,e^{-i\omega t+im\theta}, \tag{16}$$

where $\epsilon \ll 1$, $\{\hat{U},\hat{V},\hat{W},\hat{p},\hat{F}\}$ stand for the eigenmode spatial dependence of the corresponding quantities, while $\omega = \omega_r + i\omega_i$ is the eigenfrequency and m is the azimuthal wave number. Both the eigenfrequencies and the corresponding eigenmodes are calculated as a function of the governing parameters for $m = 0$ and 1. The dominant eigenmode is that with the largest growth rate ω_i. If that growth rate is positive, the base flow is unstable under the corresponding axisymmetric ($m = 0$) or lateral ($m = 1$) perturbation.

The global linear stability analysis describes the response of the base flow to small-amplitude perturbations. If the base flow is linearly unstable, the dominant mode grows exponentially with time producing perturbations that leave the linear regime. The present stability analysis does not allow one to predict the system's response in the non-linear phase. However, the growth of an axisymmetric dominant mode is expected to lead to the jetting-to-dripping transition. On the contrary, the growth of the $m = 1$ eigenmode may be saturated by the non-linear terms of the hydrodynamic equations within the experimental field of view. In this case, the linear instability will lead to finite-amplitude lateral oscillations of the liquid system (whipping regime). It is not possible to safely predict the appearance of either convective or absolute whipping in the non-linear regime from the linear stability analysis. For this reason, we will not distinguish between those whipping modes in Sec. 4.

The theoretical model was solved with a variation of the numerical method described by Herrada and Montanero (2016). The base flow and the corresponding eigenmodes are calculated with the boundary fitted method (Thompson and Warsi, 1982). The hydrodynamic equations are discretized in the transformed radial direction η using $n_\eta^\ell = 13$ and $n_\eta^g = 40$ Chebyshev collocation points (Khorrami, 1989) in the liquid and gas domains, respectively. The transformed axial direction ξ was discretized using fourth-order finite differences and $n_\xi^\ell = n_\xi^g = 1201$ equally spaced points. The grid points accumulate near the free surface (Fig. 2) where the gradients of the hydrodynamic quantities are expected to increase. The accumulation of grid points on the outer side of the free surface is important to accurately integrate the gaseous boundary layer, which plays an important role in the calculation of the $m = 1$ mode (Gordillo and Pérez-Saborid, 2005). We have verified that neither the base flow nor the eigenvalues characterizing the linear modes changed significantly when the number of grid points was increased (Fig. 3). More details of the numerical method can be found elsewhere (Herrada and Montanero, 2016).

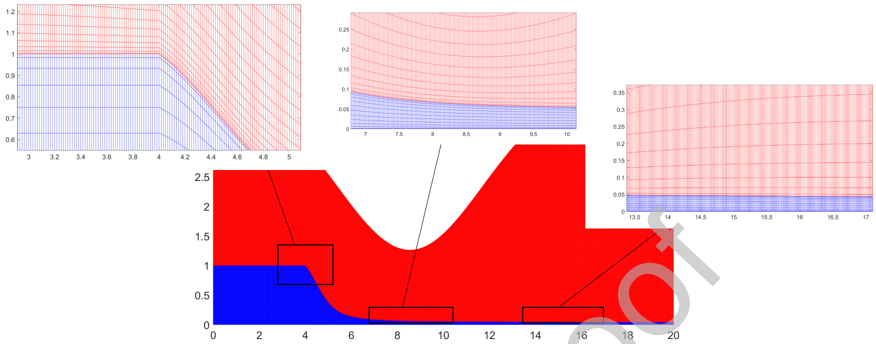

Figure 2: Details of the grid used in the simulations.

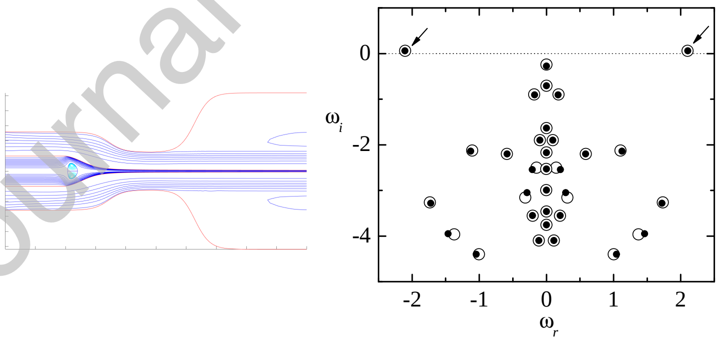

Figure 3: (Left) Streamlines of the base flow for the nozzle considered in Sec. 4.1, $H = 440$ μm, $Q = 4.2$ ml/h, and $\Delta p = 154$ mbar. (Right) Spectrum of eigenvalues for $m = 1$. The solid and open symbols correspond to ($n_\xi^\ell = n_\xi^g = 1201, n_\eta^\ell = 11$, $n_\eta^g = 31$) and ($n_\xi^\ell = n_\xi^g = 1201, n_\eta^\ell = 15, n_\eta^g = 40$), respectively.

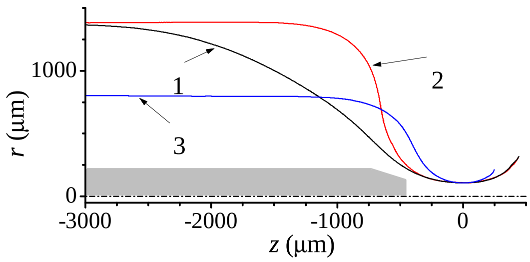

Figure 4: Inner shape of Nozzles 1, 2, and 3. The grey region shows the position of the feeding tube for $H = 450$ μm.

3. Experimental method

Three flow focusing ejectors were used in the experiments. In each of these ejectors, a tube of radius R_1=100 μm was coaxially located inside a converging-diverging nozzle. We used three nozzles with different shapes but with the same neck diameter D=220 μm. These nozzles were fire-shaped from cut-end borosilicate capillaries (Hilgenberg Gmbh) and optically characterized by the method described by Muñoz-Sánchez et al. (2019). Figure 4 shows the shapes of the nozzles and the inner capillary located at a distance H= 450 μm from the nozzle neck. Nozzles 1 and 2 were fabricated from capillaries of OD 3.3±0.1 mm and ID 2.8±0.1 mm at different heating positions. Nozzle 1 was heated deep in the flame for a short time, while Nozzle 2 was heated in an outer region for a longer time. As can be observed, the nozzles have practically the same neck diameter and shape in the diverging part. However, they exhibit significantly different shapes in front of the neck. In Nozzle 1, the diameter reduction spreads over a long region. The shape of Nozzle 2 is closer to that of the plate-orifice configuration because the diameter reduction occurs over a shorter length. The diameter reduction is large for these two nozzles. For this reason, it involved a large amount of molten material, and, consequently, the necks are long. Nozzle 3 was fabricated from a thinner capillary (OD 2.0±0.1 mm, ID 1.6±0.1 mm) and at an outer heating position. The diameter reduction is smaller in this case, and, therefore, the neck is considerably shorter. The three flow focusing ejectors used in the present study are expected to produce an intense focusing effect, which confers practical relevance upon our results.

In our experiments, the liquid was injected at a constant flow rate Q through the feeding tube by a syringe pump KDS120 (kdScientific). Air was injected across the nozzle with a constant pressure drop Δp. We observed the emitted jet using a CCD camera (AVT Stingray F-125B) equipped with optical lenses and LED backlight. The camera exposure time was reduced to 4 μs to acquired sharp images. The optical magnification was 1.295 μm/pixel. A three-axis translation stage allowed for proper alignment and focusing. All the elements were mounted on a vibration isolation board.

We examined the behavior of distilled water, 1-cSt silicone oil, and 100-cSt

	ρ_ℓ (kg/m^3)	μ_ℓ (mPa·s)	σ (mN/m)	Oh
Distilled water	998	1.00	72	0.0118
1-cSt silicone oil	818	0.818	17	0.0217
5-cSt silicone oil	971	4.60	19	0.107
100-cSt silicone oil	961	96	21	2.14

Table 1: Physical properties of the liquids considered in our study.

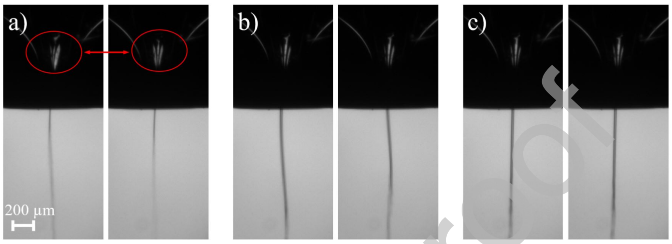

Figure 5: Absolute whipping (a), convective whipping (b), and jetting (c) in experiments with water. The red circles in (a) indicates the oscillation of the tapering meniscus.

silicone oil to analyze the influence on the stability map of both the surface tension and liquid viscosity. The values of the physical properties of the liquids considered in our study are displayed in Table 1. The table also shows the physical properties of 5-cSt silicone oil considered in the theoretical analysis of Sec. 4, and the value of the Ohnesorge number calculated with the radius R_1=100 μm of the feeding capillary.

The experimental sequence consisted of the following steps. The pressure drop was applied to the air stream. The liquid was injected at a sufficiently large flow rate to establish the jetting regime. Then, the flow rate Q was progressively reduced to determine the values corresponding to the transitions between the different regimes. This sequence was repeated for applied pressure drops in the interval $50 \leq \Delta p \leq 300$ mbar.

The images acquired in the experiments were analyzed to determine the regime adopted by the system for each pair of values Δp and Q. As explained in the Introduction, two types of whipping instabilities were distinguished (Acero et al., 2012): convective whipping in which the tapering meniscus remains stable and the emitted jet oscillates laterally, and absolute whipping in which both the meniscus and the jet oscillate. Due to the difficulties inherent to the experiment, we adopted the following simple criterion to identify the above-mentioned regimes. Absolute whipping occurs if some visible section of the meniscus (see the circle in Fig. 5a) oscillates with an amplitude larger than the jet radius. Convective whipping takes place if this oscillation occurs only beyond the discharge orifice (Fig. 5b). Finally, jetting occurs if neither of these conditions applies (Fig. 5c).

4. Theoretical results

4.1. Comparison with previous experiments

As can be observed from the comparison between Figs. 3-left and 4, the focusing geometry in our experiments is more complicated than that considered by Acero et al. (2012). We chose this geometry to enhance the focusing effect produced by the gaseous stream in the neck, which makes the results more interesting at the practical level. However, the mesh generation method used in the numerical simulations fails to adapt to the solid shapes shown in Fig. 4. For this reason, we will limit the comparison between theory and experiments to the geometry examined by Acero et al. (2012).

In this section, we assess the accuracy of the linear stability analysis by comparing its predictions with the experimental results of Acero et al. (2012). The numerical domain is that considered by Cruz-Mazo et al. (2017) (see Fig. 4 of that reference), which approximately coincides with the experimental configuration (Fig. 1). The base flow was calculated for a given flow rate and different applied pressure drops. The example in Fig. 3 shows how the drag force exerted by the outer stream causes a recirculation pattern in the liquid meniscus. The existence of this pattern prevents one from safely using 1D approximations or local stability analysis in this problem. We calculated the spectrum of eigenvalues of the modes $m = 0$ and 1 for each of the base flows. The transition from jetting to dripping (whipping) takes place when the growth rate of the dominant $m = 0$ ($m = 1$) mode becomes positive. As can be observed in Fig. 3, $\omega_r \neq 0$ in that case, which means that the instability has an oscillatory character.

Figure 6 shows the stability map obtained from the experiments of Acero et al. (2012) for 5-cSt silicone oil. The figure also shows the marginally stable numerical realizations under $m = 0$ and $m = 1$ perturbations. In all the cases analyzed, the mode $m = 2$ was stable. Three regimes are distinguished: (i) dripping, (ii) whipping in which only the jet or both the jet and the tapering meniscus oscillate laterally, and (iii) jetting in which both the tapering meniscus and the jet are stable. As explained in Sec. 2, we here do not make a distinction between convective and absolute whipping owing to the inability of the linear stability analysis to predict the type of whipping that prevails in the non-linear response of the system. The results for $H = 350$ μm agree well with the experimental data, although there is a small region of whipping in the experiments which has not been detected by the global stability analysis. The value of H is slightly smaller than that measured in the experiments ($H = 440$ μm), which may be attributed to an error in the measurement of H caused by the optical distortion produced by the significant curvature of the converging part of the micronozzle. In fact, Acero et al. (2012) conducted their experiments for a large value of H. Montanero et al. (2011) showed that the flow rate at the jetting-to-dripping transition is very sensitive to H as this parameter approaches its maximum value. Therefore, small errors in H can lead to significant errors in the critical flow rate. Another source of discrepancy is the deviation of the nozzle and feeding capillary numerical shapes from their experimental counterparts. In particular, the feeding capillary in the simulations has zero thickness

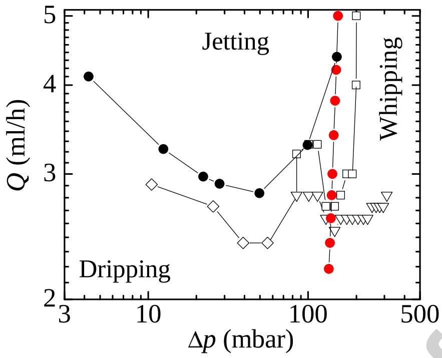

Figure 6: Stability map obtained from the experiments conducted by Acero et al. (2012) for 5-cSt silicone oil (open symbols). The open diamonds, squares, and triangules correspond to the jetting-to-dripping, jetting-to-whipping, and whipping-to-dripping transitions in the experiments. The black and red solid circles show the marginally stable flows under $m = 0$ and 1 perturbations, respectively, calculated numerically for $H = 350$ μm.

while in the experiment both the thickness and shape of the capillary end may play a significant role. In the global stability analysis, we considered two values of the capillary-to-neck distance H (Fig. 7). As can be observed, the value of H considerably affects the instability transition for $m = 0$ (Montanero et al., 2011), while it hardly alters the flow stability under the $m = 1$ perturbation.

We now analyze the eigenmodes $m = 1$ responsible for the whipping instability. We show in Fig. 8 the magnitude $|\hat{F}(z)|$ of the free surface perturbation amplitude. This amplitude monotonically grows as the distance from the feeding capillary increases. The function $|\hat{F}(z)|$ exhibits approximately the same shape in all the cases, although they probably correspond to experimental realizations of convective and absolute whipping.

4.2. Effect of the nozzle shape

Acero et al. (2012) hypothesized that the appearance of whipping in GDVN ejectors is linked to the axial component of the gas flow induced by the nozzle shape in front of the neck. To analyze the validity of this hypothesis, in this section we study the influence of an increase in the convergence rate of the focusing nozzle on the flow stability under $m = 1$ perturbations. This could have been done with the geometrical model used in Sec. 4.1. However, the mesh generation method used in our numerical simulations fails to adapt to that model when the nozzle convergence is increased. For this reason, we conducted numerical simulations with the (simpler) nozzle shape given by the expression (Fig. 9)

$$S(z) = R_o - (R_o - D/2)\exp[-\alpha(z - L_l)^2], \tag{17}$$

where all the distances have been made dimensionless with the capillary radius R_1. In these simulations, we considered 5-cSt silicone oil focused by air. The

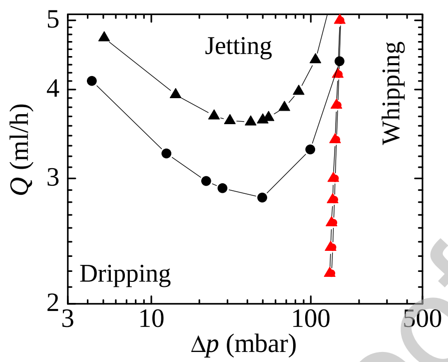

Figure 7: Marginally stable flows under $m = 0$ (black symbols) and 1 (red symbols) perturbations calculated numerically for 5-cSt silicone oil focused with the nozzle used by Acero et al. (2012). The circles and triangles correspond to $H = 350$ and 440 μm, respectively.

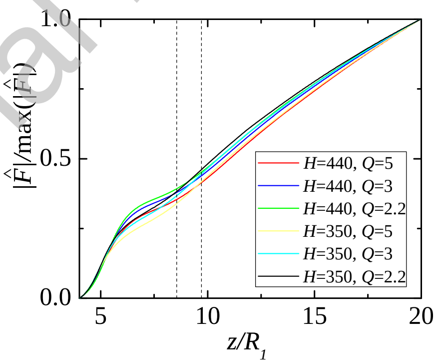

Figure 8: Magnitude of the free surface perturbation amplitude, $|\hat{F}(z)|$, corresponding to the mode $m = 1$ for the marginally stable flows in the simulations. The results have been normalized with the maximum value for each case. The labels indicate the values of the capillary-to-neck distance and flow rate measured in μm and ml/h, respectively. The vertical dashed lines show the positions of the nozzle neck for the two values of H considered.

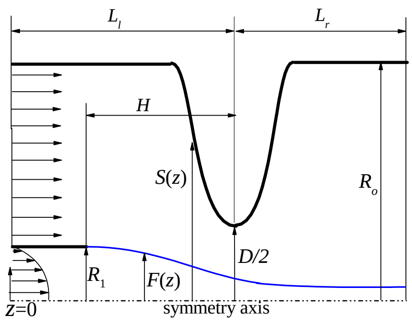

Figure 9: Sketch of the computational domain.

values of the geometrical parameters R_o, D, and L_l were the same as those in Sec. 4.1, while the capillary-to-neck distance was $H = 350$ μm ($H/R_1 = 4.55$). To analyze the effect of the convergence rate on the base flow stability, we carried out simulations for $\alpha = 0.045$, 0.05, and 5. As α increases, the nozzle shape approaches that of the plate-orifice configuration.

The effect of the nozzle convergence rate α on the whipping instability can be clearly appreciated in Fig. 10. As α increases, the pressure drop necessary to trigger the whipping instability increases. In fact, a small increase of α causes a significant increase in the critical pressure drop for the same liquid flow rate. We have not found whipping instability for $\alpha = 5$. The nozzle shape also affects the minimum flow rate leading to the growth of the dominant $m = 0$ mode (dripping). The focusing orifice thickness increases as α decreases, which generally enhances the focusing effect and reduces the minimum flow rate. Interestingly, the dependency of the minimum flow rate with respect to α is not monotonous. In fact, the stabilizing effect mentioned above is not observed when α decreases from 0.05 to 0.045, or when α decreases from 5 to 0.045 for $\Delta p \gtrsim 200$ mbar. The axial dependence of the free surface perturbation (Fig. 11) is very similar to that found for the nozzle considered in Sec. 4.1.

The neutral stability curve $m = 0$ for $\alpha = 0.045$ and 0.05 is shown to extend all the way into the region where the mode $m = 1$ becomes unstable. This means that there are parameter conditions for which both the varicose and whipping modes are unstable. In the linear regime, growing modes do not interfere with each other. If the growth rates of those modes are sufficiently different from each other, varicose (whipping) instability will be observed if the mode $m = 0$ ($m = 1$) is the dominant one. If the growth rates take similar values, then both instabilities can become noticeable at the same time. This behavior can probably be extrapolated to the nonlinear regime. In that case, we expect to observe dripping from a straight liquid thread, whipping, or dripping from a bend thread depending on the relative values of the axisymmetric and whipping growth rates. This extrapolation must be done with caution because of the

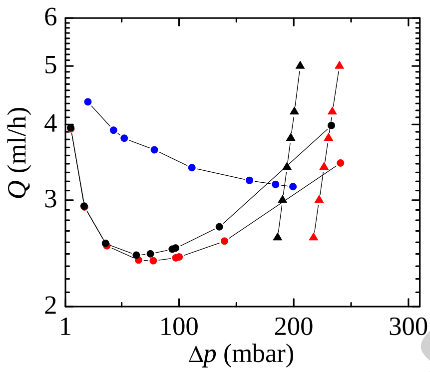

Figure 10: Stability limits under $m = 0$ (circles) and 1 (triangles) perturbations in the simulations. The results were obtained for 5-cSt silicone oil focused by air. The nozzle shape is given by the expression (17) with $\alpha = 0.045$ (black symbols), 0.05 (red symbols), and 5 (blue symbols). The whipping instability for $\alpha = 5$ was not found.

interference between growing linear modes in the nonlinear regime.

5. Experimental results

In this section, we analyze experimentally the role played by both the capillary-to-neck distance and the nozzle shape on the stability of the steady jetting regime produced by a GDVN ejector. As explained in Sec. 3, we here distinguish the experimental realizations where both the tapering meniscus and emitted jet oscillated (absolute whipping) from those in which the instability affected only the jet (convective instability) (Fig. 5). Figure 12 shows the stability regions in the Q-Δp parameter plane for distilled water focused by air in Nozzle 1 (see Sec. 3) and two different values of H. The black lines/symbols correspond to the shortest distance H=450 μm, and separate the parameter regions where jetting (J), dripping (D) and absolute whipping (AW) were observed. The red line/symbols show the jetting-to-dripping transition for H= 550 μm. The figure shows the critical role played by the air speed in the absolute whipping instability. When the pressure drop Δp is sufficiently large and the distance H takes the smallest value, the outer stream causes the meniscus oscillation. This phenomenon disappears when the feeding capillary is moved away from the nozzle neck because the gap between the capillary and the nozzle increases, and, consequently, the axial speed of the air stream surrounding the meniscus decreases. In addition, the reduction of the air speed slightly increases the flow rate at the jetting-to-dripping transition for most of the applied pressure drops.

Absolute whipping can also be prevented by selecting appropriately the shape of the nozzle. This can be done with the fire-shaping method recently developed by Muñoz-Sánchez et al. (2019). Figure 13 shows the stability regions obtained for distilled water, H=450 μm, and Nozzles 1, 2 and 3, whose necks

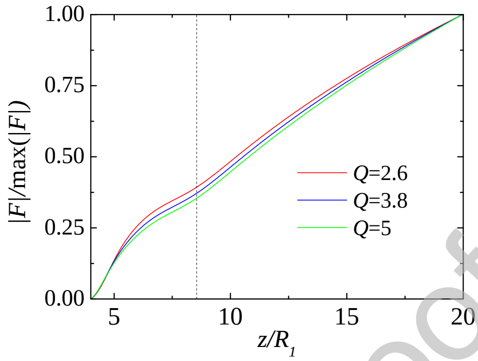

Figure 11: Magnitude of the free surface perturbation amplitude, $|\hat{F}(z)|$, corresponding to the mode $m = 1$ for the marginally stable flows in the simulations. The results have been normalized with the maximum value for each case. The labels indicate the values of the flow rate measured in ml/h. The vertical dashed line shows the position of the nozzle neck.

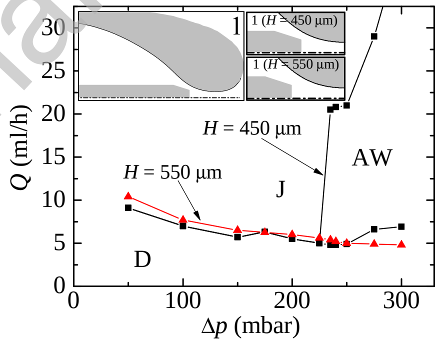

Figure 12: Experimental stability regions for water focused with air. The black and red symbols correspond to $H = 450$ and 550 μm, respectively. Neither convective nor absolute whipping was observed for $H = 550$ μm. The insets show the shape of the nozzle and the position of the feeding capillary for the two values of H considered.

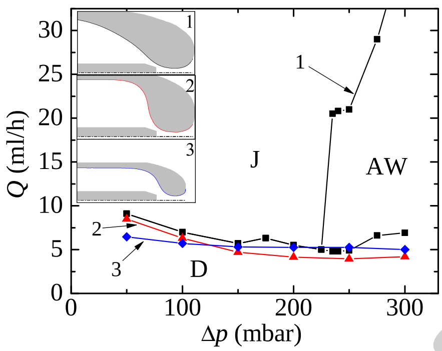

Figure 13: Experimental stability regions for water focused with air with Nozzles 1, 2 and 3. In all the cases, H=450 μm. Nozzles 2 and 3 show neither absolute nor convective whipping. The insets show the shape of the nozzle and the position of the feeding capillary.

have the same diameter. Nozzles 1 and 2 have different convergence rates (distances along which the diameter reduction takes place) but practically the same shape beyond the neck (see Fig. 4). The radial component of the velocity field in front of the neck of Nozzle 2 is expected to be larger than its counterpart in Nozzle 1. In fact, the flow pattern in Nozzle 2 must be similar to that of the classical plate-orifice configuration (Gañán-Calvo, 1998). As suggested by the stability analysis (Sec. 4.2), whipping is suppressed in Nozzle 2. Nozzle 3 is considerably smaller than the other two nozzles. Consequently, the capillary is located farther away from the nozzle inner wall for the same H. In this case, the axial component of the air velocity around the liquid meniscus is smaller, and absolute whipping is not observed.

To examine the influence of the liquid viscosity on the jetting stability, we conducted experiments with 100-cSt silicone oil. In graph (a) of Fig. 14, we compare the stability regions for the three nozzles. Absolute whipping occupies a very narrow region in the stability map. Convective whipping (CW) arises when sufficiently large pressure drops are applied to Nozzle 1. One can conclude that viscosity stabilizes the liquid meniscus in Nozzle 1 but not the emitted jet. Interestingly, and contrary to what happens to water, convective whipping disappears for $Q \gtrsim 10$ ml/h. Nozzles 2 and 3 show neither absolute nor convective whipping. Surprisingly, the nozzle shape in front of the neck affects the response of the jet far away from the discharge orifice (convective whipping). A plausible explanation for this counter-intuitive observation is that the meniscus slightly oscillates for large viscosity in Nozzle 1. This oscillation is convected and amplified downstream by the emitted jet. This would explain (i) the transition from absolute to convective instability as the viscosity increases, and (ii) the fact that convective instability is affected by the nozzle shape in front of the neck. In all the cases, the jetting-to-dripping transition takes place at flow rates much smaller than those for water. These critical flow rates hardly depend

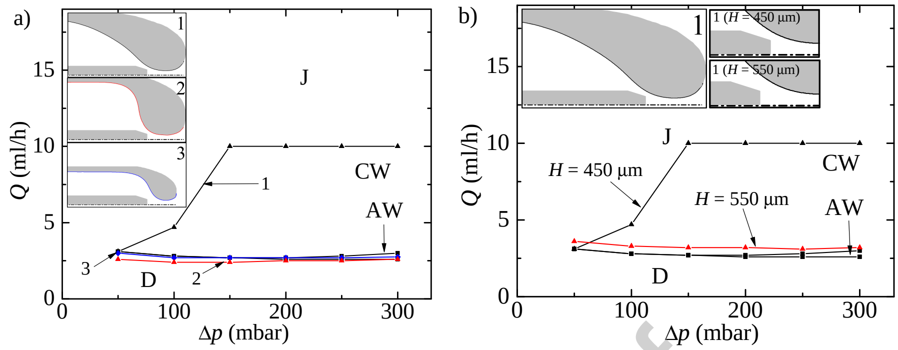

Figure 14: Experimental stability regions for 100-cSt silicone oil focused with air. a) Effect of the nozzle shape for $H = 450$ μm. Nozzles 2 and 3 show neither absolute nor convective whipping. b) Effect of the distance H for Nozzle 1. Neither convective nor absolute whipping was observed for $H = 550$ μm. The insets show the shape of the nozzle and the position of the feeding capillary.

on the applied pressure drop. In graph (b) of Fig. 14, we compare the results for Nozzle 1 and two capillary-to-neck distances: H=450 μm (black symbols) and 550 μm (red symbols). The increase of the distance H reduces the air axial velocity at the jet emission point, which eliminates the whipping instability. Overall, the liquid viscosity stabilizes the tapering meniscus by reducing the flow rate leading to the jetting-to-dripping transition, and by practically suppressing the absolute whipping. However, the minimum values of the applied pressure drop that trigger the convective whipping are considerably smaller than their counterparts in the low-viscosity case.

The role of the surface tension is examined in Fig. 15, which shows the results for 1-cSt silicone oil. This liquid has the same kinematic viscosity of water but a surface tension more than four times smaller than that of water. The main effect of the surface tension reduction is the enhancement of the absolute whipping in Nozzle 1. As explained in the Introduction, whipping arises when the difference between the pressures in the ridges and valleys of the deformed interface overcomes the stabilizing effect of the surface tension. Therefore, the reduction of the surface tension favors the whipping instability. The Weber number $\mathrm{We}_g = \rho_g(V_g - V_\ell)^2 R_i/\sigma$ compares the dynamic pressure associated with the gas velocity V_g relative to that of the liquid V_ℓ versus the capillary pressure σ/R_i in the tapering meniscus. In flow focusing, $V_\ell \ll V_g$, $\rho_g V_g^2 \sim \Delta p$, and thus $\mathrm{We}_g \sim \Delta p R_i/\sigma$. The comparison of Figs. 13 and 14 with 15 shows that the critical applied pressure for the whipping instability in Nozzle 1 has roughly decreased in the same proportion as the surface tension, which indicates that the critical Weber number takes similar values with the two liquids. The whipping instability practically prevents one from focusing low-viscosity, low-surface tension liquids with Nozzle 1. In fact, the absolute whipping observed with 1-cSt silicone oil made the tapering meniscus touch the

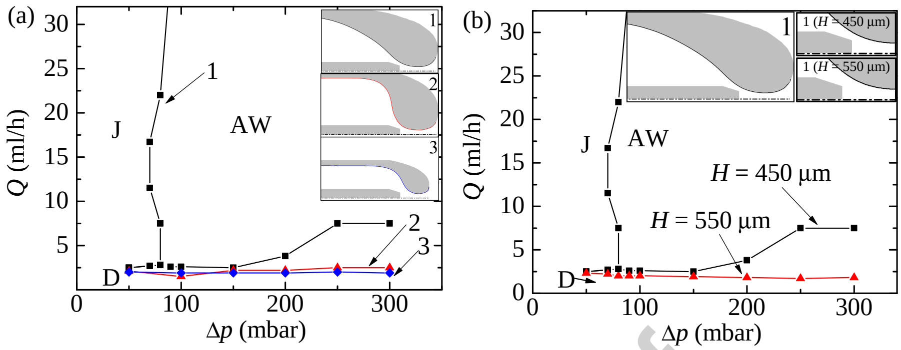

Figure 15: Experimental stability regions for 1-cSt silicone oil focused with air. a) Effect of the nozzle shape for $H = 450$ μm. Nozzles 2 and 3 show neither absolute nor convective whipping. b) Effect of the distance H for Nozzle 1. Neither convective nor absolute whipping was observed for $H = 550$ μm. The insets show the shape of the nozzle and the position of the feeding capillary.

inner wall of Nozzle 1, which continuously interrupted the liquid ejection in many experiments.

6. Conclusions

We studied the whipping instability of the tip streaming flow produced when a liquid stream is focused by a gaseous current inside a converging-diverging nozzle (GDVN ejector). We conducted the global linear stability analysis of that flow for both axisymmetric $m = 0$ and lateral $m = 1$ perturbations. For this purpose, the steady base flow was numerically calculated by solving the non-linear Navier-Stokes equations. Then, we obtain the linear eigenmodes describing the response of that flow to small-amplitude perturbations. The parameter conditions leading to dripping and whipping are assumed to be those for which the growth rate of the $m = 0$ and $m = 1$ dominant eigenmode becomes positive, respectively. The comparison with previous experimental results (Acero et al., 2012) shows good agreement for both the jetting-to-dripping and jetting-to-whipping transitions. Under the conditions considered in those experiments, the capillary-to-neck distance affects the jetting-to-dripping transition but has a negligible effect on the whipping instability. We also examined the influence of the nozzle shape on the jetting stability. Attention was paid to the nozzle convergence rate, defined as the inverse of the distance along which the diameter reduces to its minimum value. The results show that whipping is suppressed as the convergence rate increases, which explains why whipping is much less common in the classical plate-orifice configuration (Gañán-Calvo, 1998).

We also examined experimentally the influence of the ejector geometry on the jetting stability. To this end, nozzles that differed only in the convergence rate were fabricated (Muñoz-Sánchez et al., 2019). The experiments allowed us to distinguish to types of lateral instabilities: absolute and whipping instabilities depending on whether the meniscus oscillates or not, respectively (Acero et al., 2012). Absolute whipping was clearly observed only when water was focused in the nozzle with the smallest convergence rate and capillary-to-neck distance. The increase of the nozzle convergence rate and capillary-to-neck distance eliminated the whipping instability. Viscosity practically suppressed the meniscus oscillation and induced the transition from absolute to convective whipping. The increase of the convergence rate and capillary-to-neck distance eliminated the whipping instability in the high-viscosity case as well. The reduction of the surface tension decreased roughly in the same proportion the critical pressure drop for absolute whipping.

Flow focusing, as most tip streaming microfluidic realizations (Montanero and Gañán-Calvo, 2020), consists of two markedly different fluidic structures: a non-slender confined tapering meniscus and almost cylindrical emitted jet flying in a discharge environment. The steady jetting mode requires the stability of both structures. The theoretical and experimental results presented in this work show the complexity of the whipping phenomenon in flow focusing, as already pointed out by Acero et al. (2012). The stability map strongly depends on many parameter conditions, which prevents one from drawing general conclusions. For instance, the capillary-to-neck distance seems not to affect the whipping instability under the conditions considered in Fig. 6, while it plays a significant role in the present experiments [Figs. 12 and 14(b)]. There are also counter-intuitive results. For example, the liquid viscosity eliminates the whipping instability and enables the jetting regime for $Q \gtrsim 10$ ml/h (Fig. 14). Another example is that the shape of the converging part of the nozzle has a considerable effect on the response of the liquid jet far away from the discharge orifice. This last result can be understood if we assume that convective whipping does not take place because of the wind-induced destabilization of the jet downstream, but due to the convection and amplification of lateral waves emitted by small-amplitude oscillations of the liquid meniscus. Overall, we can probably conclude that ejector shapes closer to the plate-orifice configuration are less prone to producing whipping.

Acknowledgements

Partial support from the Ministerio de Economía y Competitividad and Gobierno de Extremadura (Spain) through Grant Nos. DPI2016-78887 and GR18175 are gratefully acknowledged.

References

Acero, A.J., Ferrera, C., Montanero, J.M., Gañán-Calvo, A.M., 2012. Focusing liquid microjets with nozzles. J. Micromech. Microeng. 22, 065011.

Anna, S.L., Mayer, H.C., 2006. Microscale tipstreaming in a microfluidic flow focusing device. Phys. Fluids 18, 121512.

Beyerlein, K.R., Adriano, L., Heymann, M., Kirian, R., Knoska, J., Wilde, F., Chapman, H.N., Bajt, S., 2015. Ceramic micro-injection molded nozzles for serial femtosecond crystallography sample delivery. Rev. Sci. Instrum. 86, 125104.

Castro-Hernández, E., Gundabala, V., Fernández-Nieves, A., Gordillo, J.M., 2009. Scaling the drop size in coflow experiments. New J. Phys. 11, 075021.

Chapman *et al.*, H.N., 2011. Femtosecond X-ray protein nanocrystallography. Nature 470, 73–79.

Chigier, N., Reitz, R.D., 1996. Regimes of jet breakup and breakup mechanisms (physical aspects), in: Recent Advances in Spray Combustion: Spray Atomization and Drop Burning Phenomena, AIAA, Reston. pp. 109–135.

Cohen, I., Li, H., Hougland, J.L., Mrksich, M., Nagel, S.R., 2001. Using selective withdrawal to coat microparticles. Science 292, 265–267.

Collins, R.T., Jones, J.J., Harris, M.T., Basaran, O.A., 2008. Electrohydrodynamic tip streaming and emission of charged drops from liquid cones. Nature Phys. 4, 149–154.

Cruz-Mazo, F., Herrada, M.A., Gañán-Calvo, A.M., Montanero, J.M., 2017. Global stability of axisymmetric flow focusing. J. Fluid Mech. 832, 329–344.

DePonte, D.P., Weierstall, U., Schmidt, K., Warner, J., Starodub, D., Spence, J.C.H., Doak, R.B., 2008. Gas dynamic virtual nozzle for generation of microscopic droplet streams. J. Phys. D: Appl. Phys. 41, 195505.

Dharmansh, D., Chokshi, P., 2016. Axisymmetric instability in a thinning electrified jet. Phys. Rev E 93, 043124.

Dharmansh, D., Chokshi, P., 2017. Stability analysis of an electrospinning jet of a polymeric fluid. Polymer 131, 34–49.

Eggers, J., 1997. Nonlinear dynamics and breakup of free-surface flows. Rev. Mod. Phys. 69, 865–929.

Eggers, J., Villermaux, E., 2008. Physics of liquid jets. Rep. Prog. Phys. 71, 036601.

Forbes, T.P., Sisco, E., 2014a. Chemical imaging of artificial fingerprints by desorption electro-flow focusing ionization mass spectrometry. Analyst 139, 2982.

Forbes, T.P., Sisco, E., 2014b. Mass spectrometry detection and imaging of inorganic and organic explosive device signatures using desorption electro-flow focusing ionization. Anal. Chem. 86, 7788–7797.

Gañán-Calvo, A.M., 1998. Generation of steady liquid microthreads and micron-sized monodisperse sprays in gas streams. Phys. Rev. Lett. 80, 285–288.

Gañán-Calvo, A.M., López-Herrera, J.M., Riesco-Chueca, P., 2006. The combination of electrospray and flow focusing. J. Fluid Mech. 566, 421–445.

Gañán-Calvo, A.M., Montanero, J.M., Martín-Banderas, L., Flores-Mosquera, M., 2013. Building functional materials for health care and pharmacy from microfluidic principles and Flow Focusing. Adv. Drug Delivery Rev. 65, 1447–1469.

Gordillo, J.M., Pérez-Saborid, M., 2005. Aerodynamic effects in the break-up of liquid jets: on the first wind-induced break-up regime. J. Fluid Mech. 541, 1–20.

Gordillo, J.M., Sevilla, A., Campo-Cortés, F., 2014. Global stability of stretched jets: conditions for the generation of monodisperse micro-emulsions using coflows. J. Fluid Mech. 738, 335–357.

Herrada, M.A., Montanero, J.M., 2016. A numerical method to study the dynamics of capillary fluid systems. J. Comput. Phys. 306, 137–147.

Herrada, M.A., Montanero, J.M., Ferrera, C., Gañán-Calvo, A.M., 2010. Analysis of the dripping-jetting transition in compound capillary jets. J. Fluid Mech. 649, 523–536.

Hofmann, E., Krüger, K., Haynl, C., Scheibel, T., Trebbin, M., Förster, S., 2018. Microfluidic nozzle device for ultrafine fiber solution blow spinning with precise diameter control. Lab Chip 18, 2225–2234.

Khorrami, M.R., 1989. Application of spectral collocation techniques to the stability of swirling flows. J. Comput. Phys. 81, 206–229.

Lasheras, J.C., Hopfinger, E.J., 2000. Liquid jet instability and atomization in a coaxial gas stream. Annu. Rev. Fluid Mech. 32, 275–308.

Montanero, J.M., Gañán-Calvo, A.M., 2020. Dripping, jetting and tip streaming. Rep. Prog. Phys. in press.

Montanero, J.M., Rebollo-Muñoz, N., Herrada, M.A., Gañán-Calvo, A.M., 2011. Global stability of the focusing effect of fluid jet flows. Phys. Rev. E 83, 036309.

Muñoz-Sánchez, B.N., Gañán-Calvo, A.M., Cabezas, M.G., 2019. A new fire shaping approach to produce highly axisymmetric and reproducible nozzles. J. Mater. Process. Tech. 270, 241–253.

Piotter, V., Klein, A., Plewa, K., Beyerlein, K.R., Chapman, H.N., Bajt, S., 2018. Development of a ceramic injection molding process for liquid jet nozzles to be applied for X-ray free-electron lasers. Microsyst. Technol. 24, 1247–1252.

Ponce-Torres, A., Montanero, J.M., Vega, E.J., Gañán-Calvo, A.M., 2016. The production of viscoelastic capillary jets with gaseous flow focusing. J. Non-Newtonian Fluid Mech. 229, 8–15.

Ponce-Torres, A., Ortega, E., Rubio, M., Rubio, A., Vega, E.J., Montanero, J.M., 2019. Gaseous flow focusing for spinning micro and nanofibers. Polymer 178, 121623.

Ponce-Torres, A., Vega, E.J., Castrejón-Pita, A.A., Montanero, J.M., 2017. Smooth printing of viscoelastic microfilms with a flow focusing ejector. J. Non-Newtonian Fluid Mech. 249, 1–7.

Sauter, U.S., Buggisch, H.W., 2005. Stability of initially slow viscous jets driven by gravity. J. Fluid Mech. 533, 237–257.

Si, T., Li, F., Yin, X.Y., Yin, X.Z., 2009. Modes in flow focusing and instability of coaxial liquid-gas jets. J. Fluid Mech. 629, 1–23.

Si, T., Li, G.B., an Z. Q. Zhu, Q.W., Luo, X.S., Xu, R.X., 2016. Optical droplet vaporization of nanoparticle-loaded stimuli-responsive microbubbles. Appl. Phys. Lett. 108, 111109.

Stan *et al.*, C.A., 2016. Liquid explosions induced by X-ray laser pulses. Nat. Phys. 12, 966–971.

Tammisola, O., Lundell, F., Soderberg, L.D., 2012. Surface tension-induced global instability of planar jets and wakes. J. Fluid Mech. 713, 632–658.

Taylor, G., 1964. Disintegration of water drops in electric field. Proc. R. Soc. Lond. A 280, 383–397.

Theofilis, V., 2011. Global linear instability. Annu. Rev. Fluid Mech. 43, 319–352.

Thompson, J.F., Warsi, Z.U.A., 1982. Boundary-fitted coordinate systems for numerical solution of partial differential equations-a review. J. Comput. Phys. 47, 1–108.

Vasireddi, R., Kruse, J., Vakili, M., Kulkarni, S., Keller, T.F., Monteiro, D.C..F., Trebbi, M., 2019. Solution blow spinning of polymer/nanocomposite micro-/nanofibers with tunable diameters and morphologies using a gas dynamic virtual nozzle. Sci. Rep. 9, 14297.

Vega, E.J., Montanero, J.M., Herrada, M.A., Gañán-Calvo, A.M., 2010. Global and local instability of flow focusing: The influence of the geometry. Phys. Fluids 22, 064105.

Wiedorn *et al.*, M.O., 2018. Megahertz serial crystallography. Nat. Commun. 9, 4025.

Zahoor, R., Bajt, S., Sarler, B., 2018. Influence of gas dynamic virtual nozzle geometry on micro-jet characteristics. Int. J. Multiphase Flow 104, 152–165.

Declaration of interests

The authors declare that they have no known competing financial interests or personal relationships that could have appeared to influence the work reported in this paper.

Author Statement

Sergio Blanco-Trejo: Investigation,
Miguel A. Herrada: Software.
Alfonso M. Gañán-Calvo: Supervision.
Alejandro Rubio: Investigation.
María G. Caberzas: Supervision.
José M. Montanero: Supervision, Writing-Original draft preparation.